

TomoFluid: Reconstructing Dynamic Fluid from Sparse View Videos (Supplementary material)

Guangming Zang¹ Ramzi Idoughi¹ Congli Wang¹ Anthony Bennett¹ Jianguo Du¹
Scott Skeen² William L. Roberts¹ Peter Wonka¹ Wolfgang Heidrich¹
¹KAUST ²Sandia National Laboratories

1. Additional results

In this section, we provide more experimental results for the datasets shown in the main paper.

1.1. Synthetic Data

The table with PSNR/SSIM measurements at additional novel views for each approach are presented in Table 1. As stated in our submission, the best results can be achieved by our method, comparing to all baseline methods. At the same time, we can also observe that for all methods, the performance is getting better when the viewing degree is closer to the provided angle (*i.e.* at 0°, 45°, and 90°).

Table 1: PSNR/SSIM measurements for each approach. The value is averaged for projection images over all 92 time steps at the specified viewing angle (given in degrees). For each approach, average measurements for all generated projections (Avg. Proj.) and all reconstructed volumes (Avg. Vol.) are also presented.

Method	05°	15°	25°	35°	55°	65°	75°	85°	Avg. Proj.	Avg. Vol.
SART	32.16 / .872	27.55 / .846	26.02 / .852	28.25 / .896	29.97 / .905	27.00 / .859	27.15 / .837	31.35 / .862	29.43 / .868	25.54 / .505
Getreuer [2]	32.40 / .879	27.58 / .856	26.03 / .857	28.33 / .897	30.06 / .897	27.02 / .867	27.18 / .847	31.45 / .890	29.56 / .876	25.58 / .512
Okabe <i>et al.</i> [4]	29.80 / .871	26.82 / .832	25.96 / .807	27.89 / .829	27.36 / .814	25.82 / .803	26.97 / .851	31.76 / .913	28.23 / .843	25.24 / .467
Zang <i>et al.</i> [9]	32.69 / .923	28.59 / .895	27.15 / .883	28.74 / .903	30.04 / .909	28.01 / .882	28.36 / .881	31.69 / .911	29.81 / .905	25.76 / .538
Ours	36.55 / .978	30.09 / .936	28.80 / .923	31.17 / .946	32.12 / .958	29.13 / .927	29.24 / .928	34.02 / .966	32.36 / .950	27.72 / .671

In Figure 1, additional comparisons between each approach are provided. From top to bottom, results at different time frames (26, 60, and 90) are provided. Figure 1(a) presents the generated projections for each approach, while the reconstructed density volumes are provided in Figure 1(b).

1.2. Studies of input with difference of 90 °

We conduct additional quantitative and qualitative analysis of the cases that two input images have an angle difference of 90 degrees from each other. As shown in Figure 2, a lower quality results can be observed, comparing to the cases where three input images(at 0°, 45°, and 90°, respectively). The average PSNR and SSIM are 23.15 and 0.821.

1.3. Real Captured Data

In this part, we show more experimental results for the real captured data. From Figure 3 to Figure 6, we show respectively the additional results for soot, fluid, spray [1], and flame. Results for all time frames are presented in the supplementary video.

1.4. Comparison with optimal transport based method [5]

We extensively evaluate our novel view regularizer (NVR) with the optimal-transport based interpolation methods (OT), which intuitively is more physically motivated. However, as shown in Figure 7, the proposed flow based warping operations outperform the optimal-transport based method [5] for estimating the missing views, in terms of both visually comparison, numerical evaluation (absolute error of L1 norm), and running time for estimating one missing view (Our methods takes

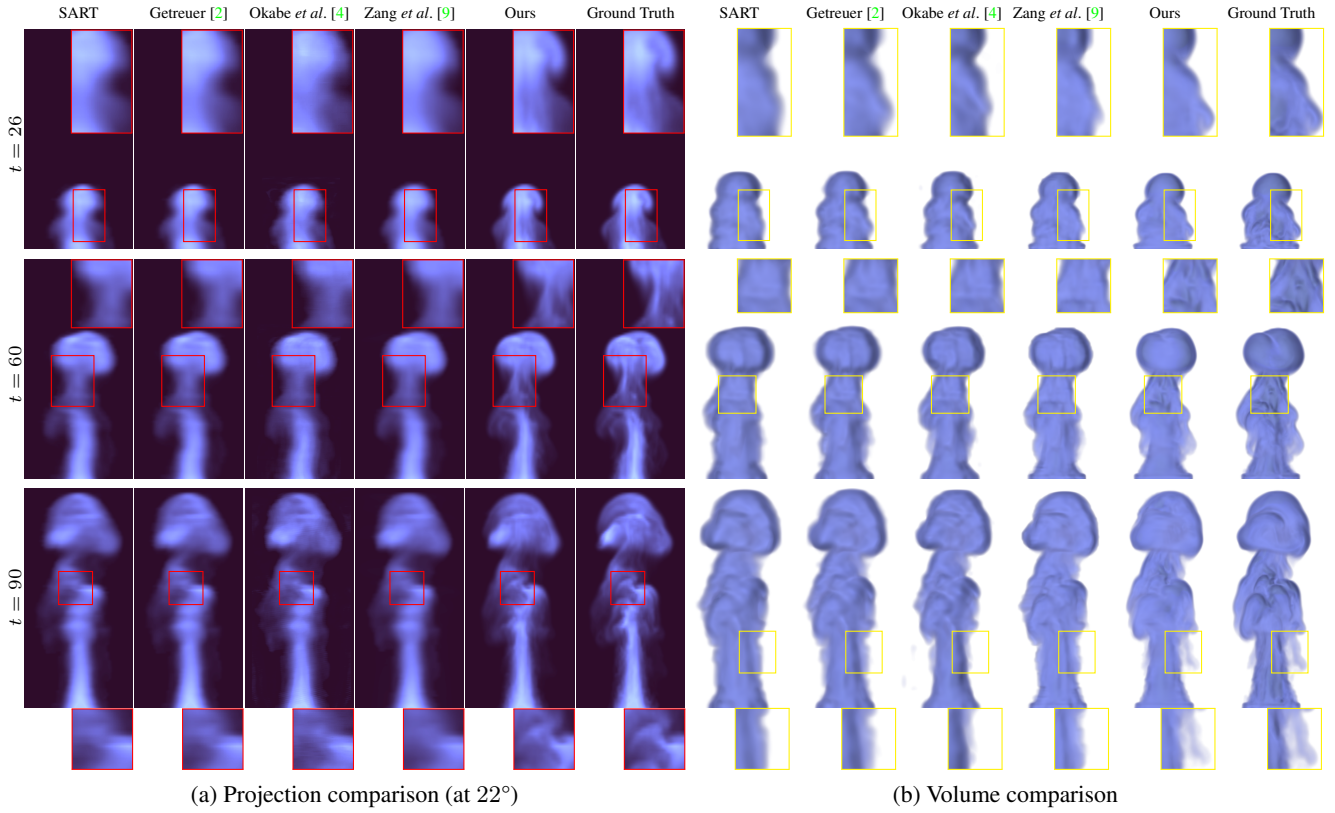


Figure 1: Comparison for different methods via projection image (a) and volume (b) visualization.

5.58 s while OT [5] takes 36.25 s for that). Different smoothing kernels ($k = 1$ and 3) in OT [5] are provided for comparison.

2. Implementation details

2.1. Parameters

Some parameters are fixed for all the datasets. In the density field reconstruction stage, β is set as 0.01, which in practice ensures a fast convergence for the algorithm. Ranging from 0.05 to 0.25 for α yields accurate results in practice. The relax factor for inner PSART algorithm [7, 8] is set as 0.3, while the number of inner iterations for PSART (# Inner) is shown in Table 2. In the flow estimation stage (Algorithm 1), 3 levels of pyramid scale are applied and the accuracy tolerance is $1e^{-4}$. The Gaussian width λ_{smooth} and cubic downsampling factor λ_{resize} are respectively 0.5 and 0.65, ζ is set as 0 for spray experiment, since the assumption of incompressible flow is not satisfied in this case. Other parameters for each dataset are provided in Table 2.

Table 2: Parameters used in the acquisition and for the optimization. The total run times ([h:mm]), summed over all outer iterations for density volume reconstruction (x-problem) and flow field estimation (u-problem) are presented.

Dataset	N	im. size	im. pixel	T	Volume size	Vox. pitch	α	γ	δ	ζ	# Outer	# Inner	x-problem	u-problem
soot	3	536×768	0.075	180	100×150×100	0.40	0.05	0.1	0.12	0.1	10	2	2:48	7:25
flame	3	408×688	0.200	100	160×275×160	0.40	0.1	0.1	0.15	0.1	15	3	2:22	5:25
fluid	2	412×706	0.200	100	150×300×150	0.50	0.2	0.3	0.15	0.1	15	2	4:15	5:24
spray	3	552×512	0.142	060	150×110×150	0.50	0.1	0.2	0.20	0.0	12	3	1:40	2:42

2.2. Details of reconstruction algorithm

We show the pseudocode for solving the \mathbf{x} (Algorithm 3) and \mathbf{u} (Algorithm 1) subproblems, respectively.

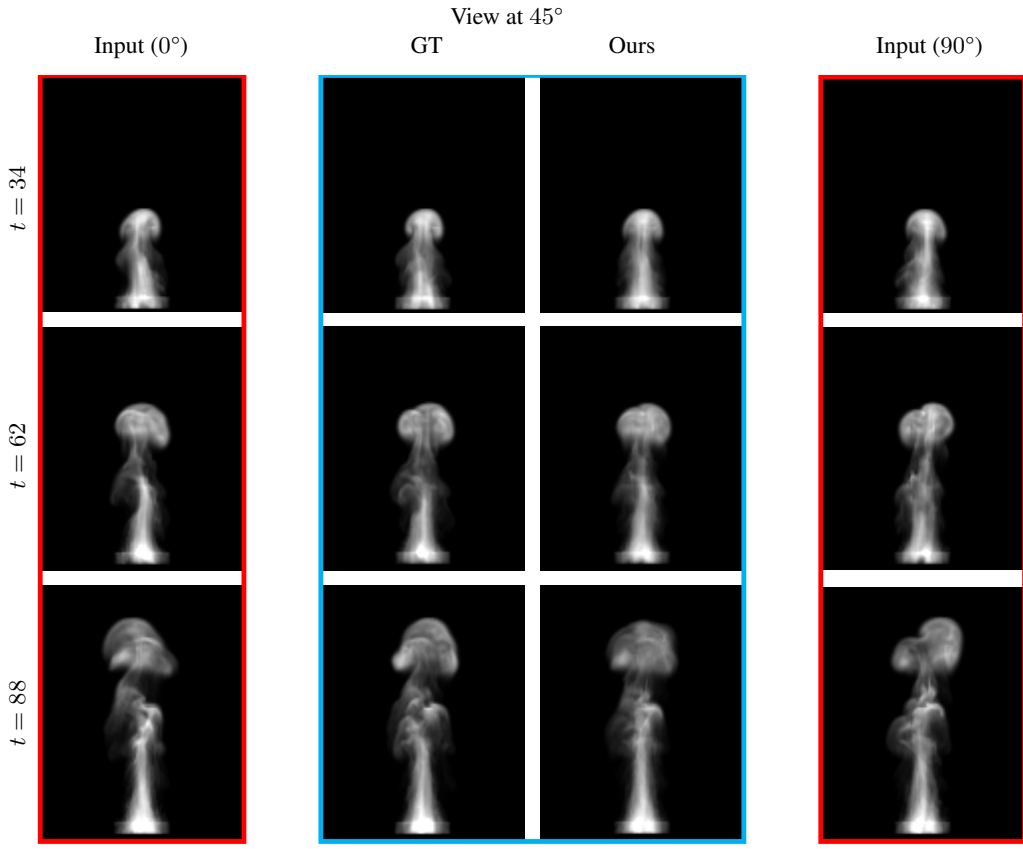


Figure 2: Two input views at 0 and 90 degrees are shown respectively at left and right (in red box). The reference inbetween projection and ours are presented. From top to bottom: images at different time frames.

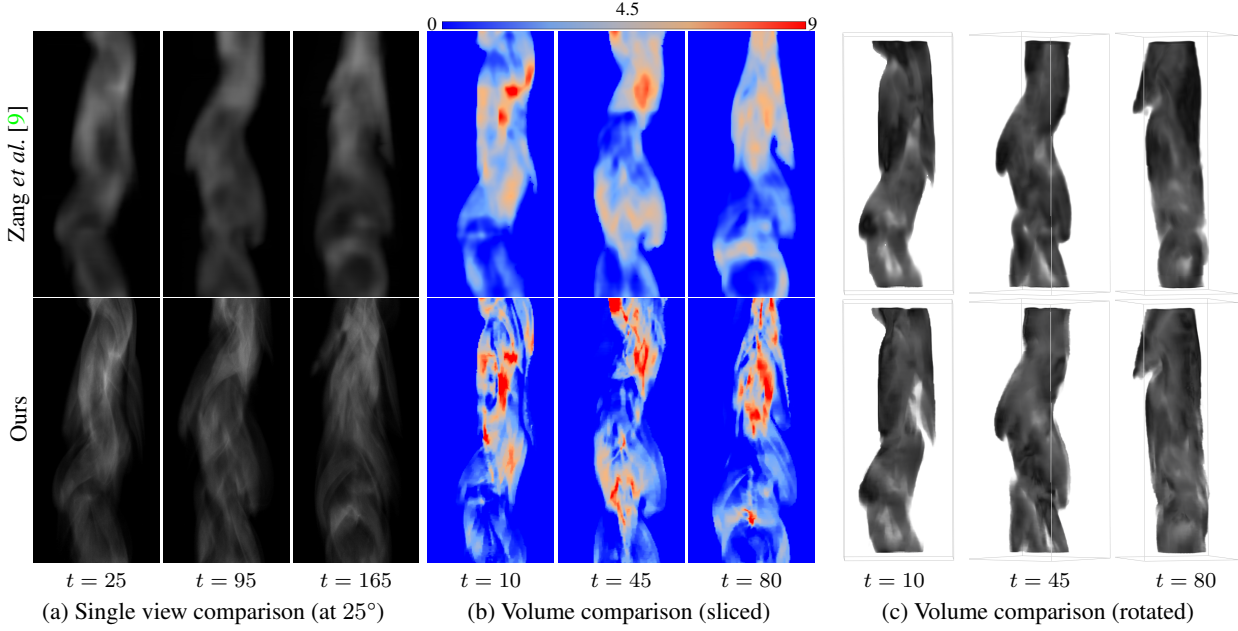


Figure 3: Reconstruction results for soot data.

3. Failure case

In this section, we show a failure case in Figure 8 for proposed method with a toy car, which is captured using a Nikon CT scanner. We can see that our proposed novel view regularizer (NVR) does not work well (see car bumper area at 40°and 43°)

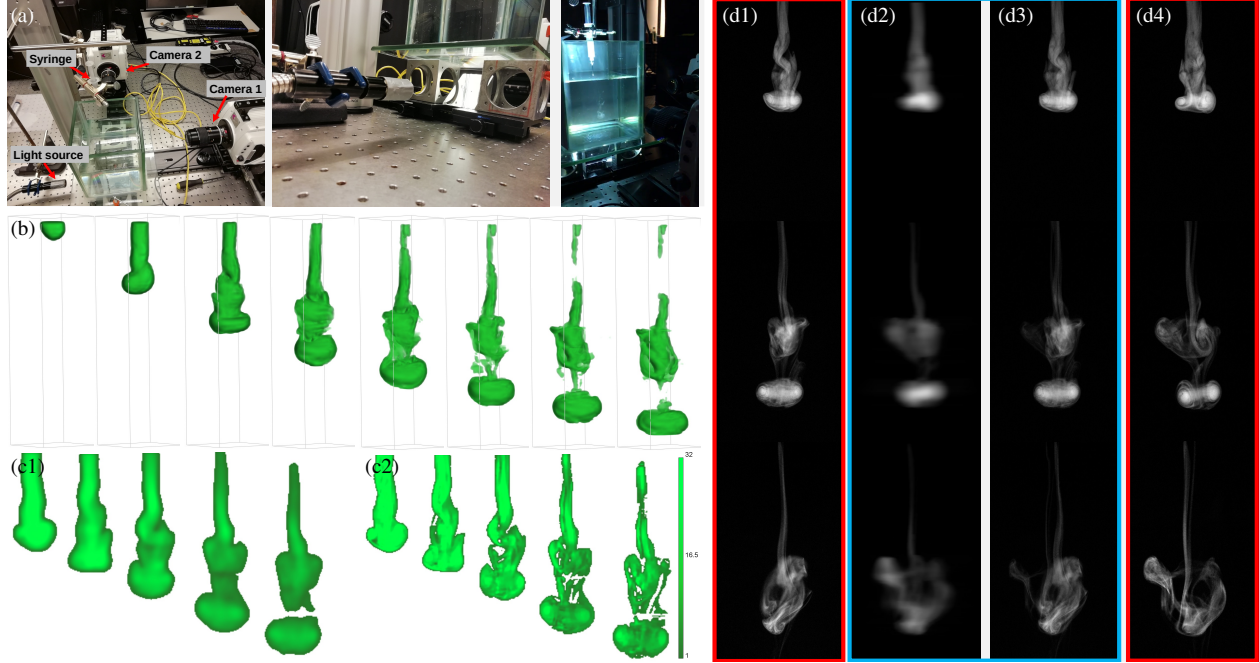


Figure 4: (a) The set up for capturing fluid imaging. (b) Reconstructed volumes from our method, viewing from the most challenge angle. (c1) reconstructed volume slice from the state-of-the-art dynamic tomographic reconstruction [9] method and ours (c2). Input projection images captured at 0° (d1) and 90° (d4). The estimated missing projection images at 30° from [9] and ours are shown in (d2) and (d3), respectively.

Algorithm 1 Pyramidal Flow Estimation (Solve line 10 in Tomofluid algorithm)

Require: $\mathbf{x}_t, \mathbf{x}_{t+1}, \lambda_{\text{smooth}}, \mathbf{y}_x, \mathbf{y}_y, \mathbf{y}_z, \lambda_{\text{resize}}, \text{ROI}_t^{l+1}, tol, n_w, \gamma$

- 1: // Gaussian smooth and downsampling input volume at frame t and $t + 1$
- 2: $(\mathbf{x}_t, \mathbf{x}_{t+1}, \text{ROI}_{t+1}) \leftarrow \text{GaussianSmooth}(\mathbf{x}_t, \mathbf{x}_{t+1}, \text{ROI}_{t+1}, \lambda_{\text{smooth}})$
- 3: **while** $l < \text{scales}$ **do**
- 4: $(\mathbf{x}_t^{l+1}, \mathbf{x}_{t+1}^{l+1}, \text{ROI}_{t+1}^{l+1}) \leftarrow \text{CubicDownsampling}(\mathbf{x}_t^l, \mathbf{x}_{t+1}^l, \text{ROI}_{t+1}^l, \lambda_{\text{resize}})$
- 5: **end while**
- 6: Initialize

- 7: **for** l from scales to 1 **do**
- 8: //Primal dual iterations for retrieving the velocity at each level.
- 9: $(\mathbf{u}_t, \mathbf{y}_x, \mathbf{y}_y, \mathbf{y}_z, \mathbf{y}_c) \leftarrow \text{EstimateVelocity}(\mathbf{x}_t^{l+1}, \mathbf{x}_{t+1}^{l+1}, \mathbf{u}_t, \mathbf{y}_x, \mathbf{y}_y, \mathbf{y}_z, \mathbf{y}_c, \text{ROI}_t^{l+1}, tol, n_w, \gamma)$
- 10: $(\mathbf{u}_t, \mathbf{y}_x, \mathbf{y}_y, \mathbf{y}_z, \mathbf{y}_c) \leftarrow \text{CubicUpsampling}(\mathbf{u}_t, \mathbf{y}_x, \mathbf{y}_y, \mathbf{y}_z, \mathbf{y}_c, \frac{1}{\lambda_{\text{resize}}})$
- 11: **end for**
- return** \mathbf{u}_t

for this data, since our observations for fluid data are not valid and no flow motion can be easily detected in this area from the two input images.

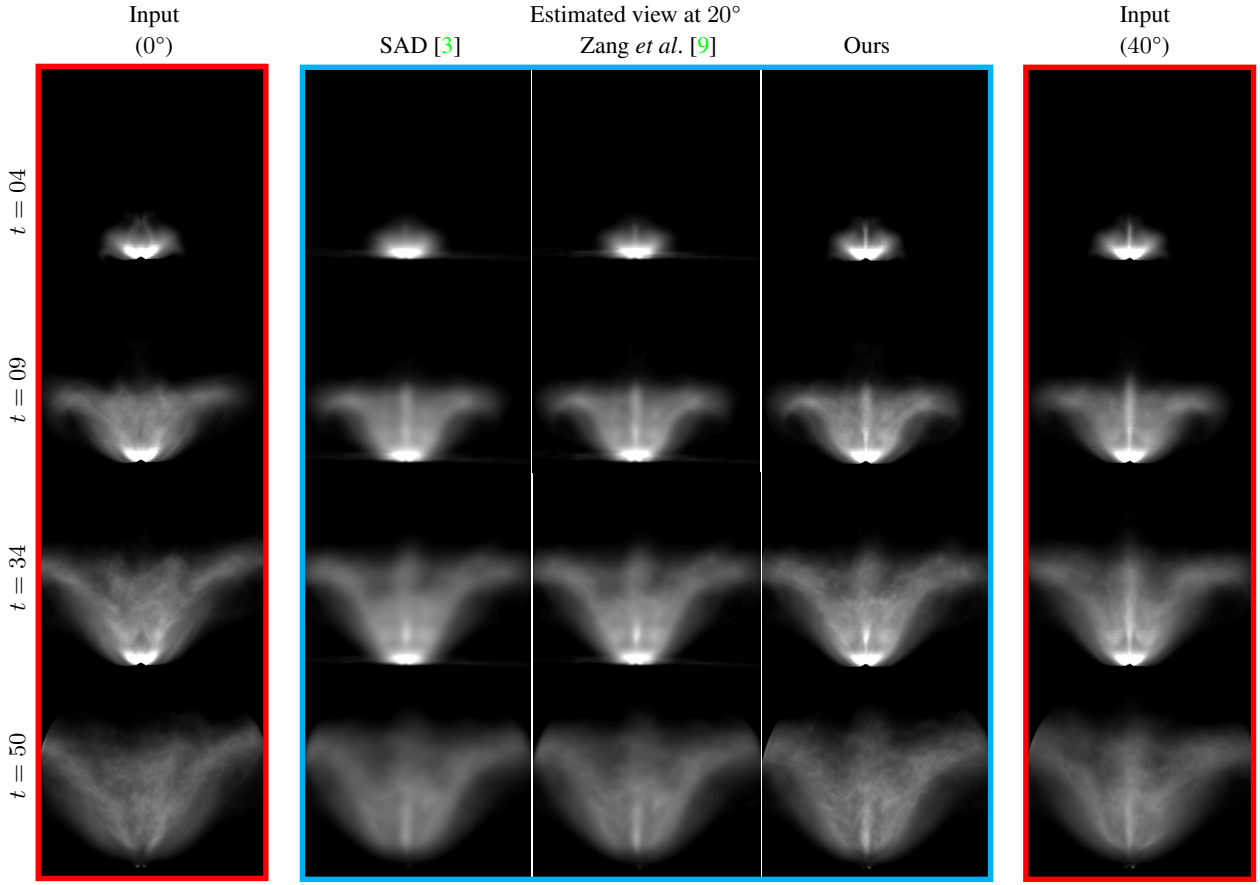


Figure 5: Two input views at 0 and 90 degrees are shown respectively at left and right (in red box). The estimated inbetween projection with SAD [3], Zang *et al.* [9], and ours are presented. From top to bottom: images at different time frames.

Algorithm 2 EstimateVelocity

Require: $\mathbf{x}_t^{l+1}, \mathbf{x}_{t+1}^{l+1}, \mathbf{u}_t, \mathbf{y}_x, \mathbf{y}_y, \mathbf{y}_z, \mathbf{y}_c, \text{ROI}_t^{l+1}, tol, n_w, \gamma$

- 1: **for** w from 1 to n_w **do**
- 2: $\text{Vol}_{\text{warp}}^w \leftarrow \text{Warp}(\mathbf{u}_t, \mathbf{x}_t^{l+1}, t)$
- 3: $\text{Vol}_{\text{grad}}^w \leftarrow \text{Gradient}(\mathbf{u}_t, \mathbf{x}_t^{l+1}, t)$
- 4: $\tilde{\mathbf{u}}_t \leftarrow \text{Vol}_{\text{warp}}^w - \mathbf{x}_t^{l+1} - \text{Vol}_{\text{grad}}^w \cdot \mathbf{u}_t$
- 5: $\mathcal{R} \leftarrow \text{OperatorConstruct}(\mathbf{x}_t^{l+1}, \mathbf{x}_{t+1}^{l+1}, \text{Vol}_{\text{grad}}^w)$
- 6: **repeat**
- 7: //slack variable update
- 8: $\mathbf{y}_i \leftarrow \text{prox}(\mathcal{R}, \mathbf{y}_i, \mathbf{z}, \sigma), i=\mathbf{x}, \mathbf{y}, \mathbf{z}, \mathbf{c}$
- 9: $\mathbf{u}_{\text{prev}} \leftarrow \mathbf{u}$
- 10: $\mathbf{u}_t \leftarrow \text{prox}(\mathcal{R}^T, \mathbf{u}_t, \tau, \tilde{\mathbf{u}}_t)$
- 11: // divergence free
- 12: $\mathbf{u}_t \leftarrow \Pi_{\text{DIV}}(\mathbf{u}_t)$
- 13: $\mathbf{z} \leftarrow 2\mathbf{u}_t - \mathbf{u}_{\text{prev}}$
- 14: **until** Converge
- 15: **end for**

return $\mathbf{u}_t, \mathbf{y}_x, \mathbf{y}_y, \mathbf{y}_z, \mathbf{y}_c$

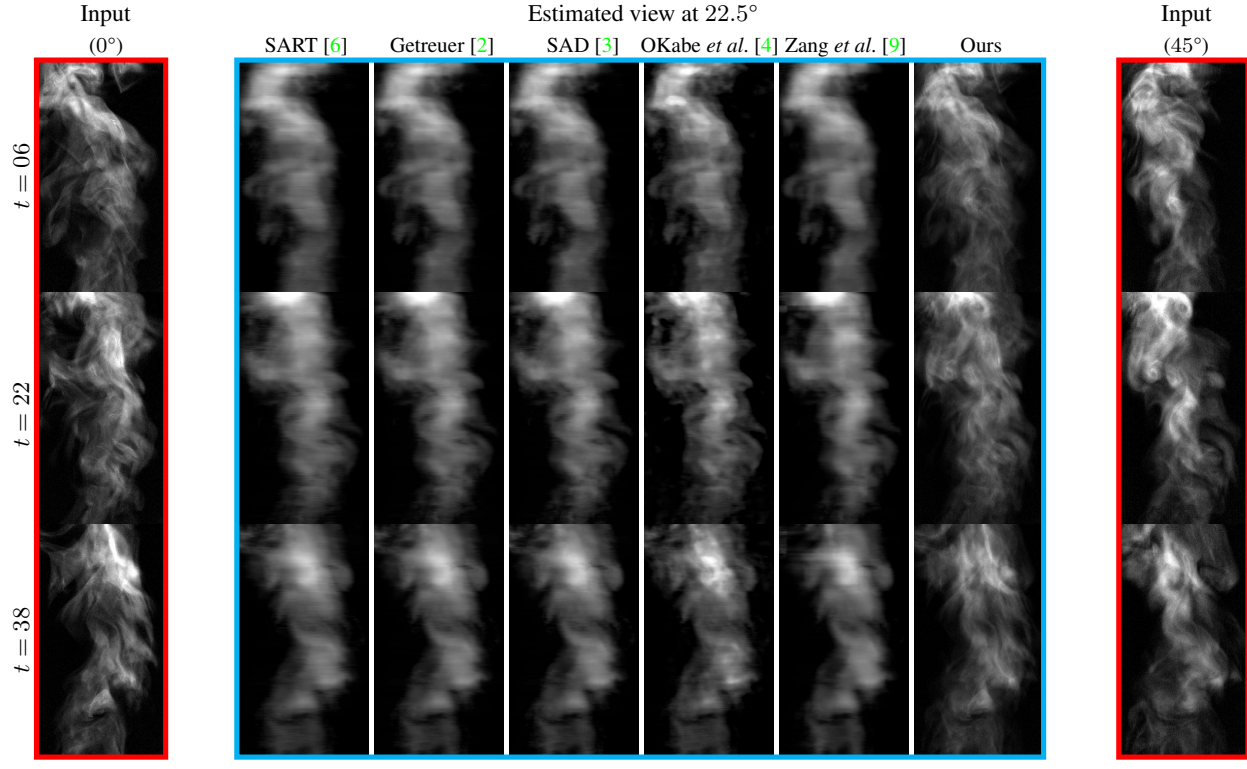


Figure 6: Comparison for flame data. Two input views at 0 and 45 degrees are shown respectively at left and right (in red box). The estimated inbetween projection with SART [6], Getreuer [2], SAD [3], OKabe *et al.* [4], Zang *et al.* [9], and ours are presented. From top to bottom: images at different time frames.

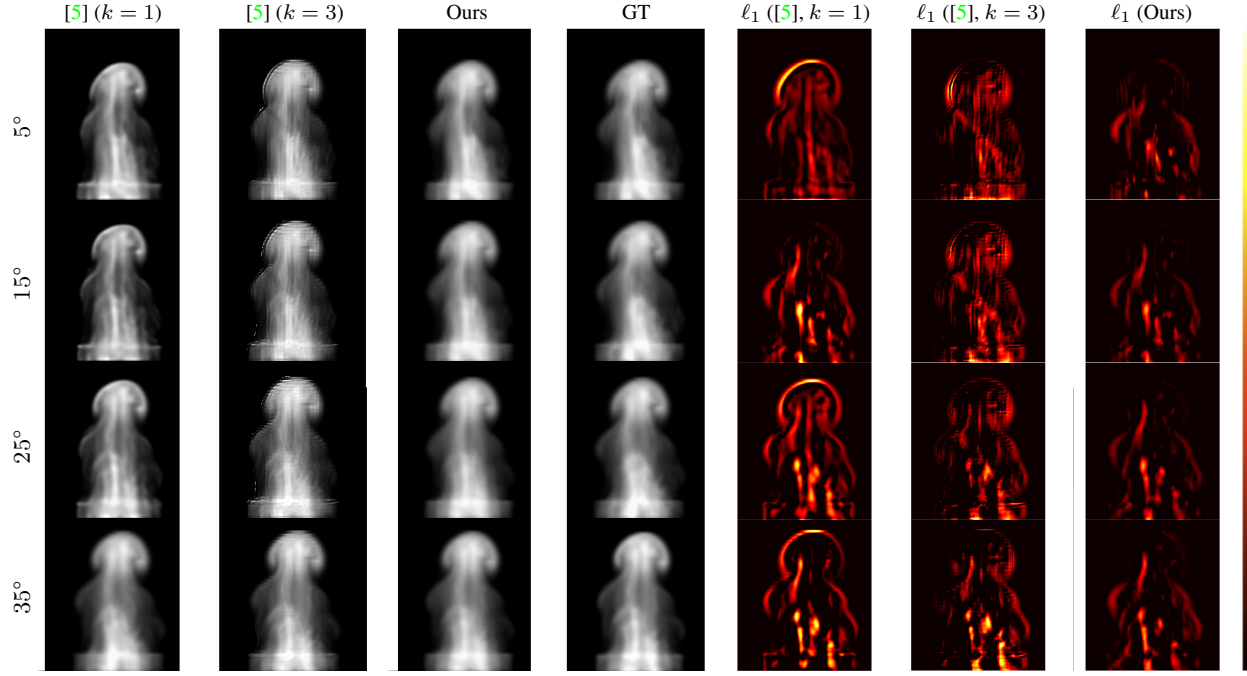


Figure 7: Comparison between OT [5], and Ours.

Algorithm 3 Visible Light Tomography (Solve line 8 in Tomofluid algorithm)

Require: $\mathbf{x}_t, \mathbf{x}_{t+1}, \mathbf{u}_t, \alpha_1, \alpha_2$

```

1: // Different iterations
2: for all  $r = 1 \dots R$  do
3:   repeat
4:      $K \leftarrow \text{OperatorConstruct}(\mathbf{x}_t^{(r)}, \mathbf{x}_{t+1}^{(r)}, \mathbf{u}_t)$ 
5:      $\bar{\mathbf{z}} \leftarrow \mathbf{z}^{(r)} + \alpha_1 K \bar{\mathbf{x}}^{(r)}$ 
6:      $\mathbf{z}^{(r+1)} \leftarrow \bar{\mathbf{z}} - \alpha_1 \text{prox}_{\frac{1}{\alpha_1} g}(\frac{\bar{\mathbf{z}}}{\alpha_1})$ 
7:      $\mathbf{x}^{(r+1)} \leftarrow \text{prox SART}_{\alpha_2 f}(\mathbf{x}^{(r)} - \alpha_2 K^T \mathbf{z}^{(r+1)})$ 
8:      $\mathbf{x}^{(r+1)} \leftarrow \Pi_{\text{Reproject}}(\mathbf{x}^{(r+1)})$ 
9:      $\mathbf{x}^{(r+1)} \leftarrow \Pi_{\text{NonNeg}}(\mathbf{x}^{(r+1)})$ 
10:     $\bar{\mathbf{x}}^{(r+1)} \leftarrow 2 \cdot \mathbf{x}^{(r+1)} - \mathbf{x}^{(r)}$ 
11:  until Converge
12: end for
  return  $\mathbf{x}_t$ 

```

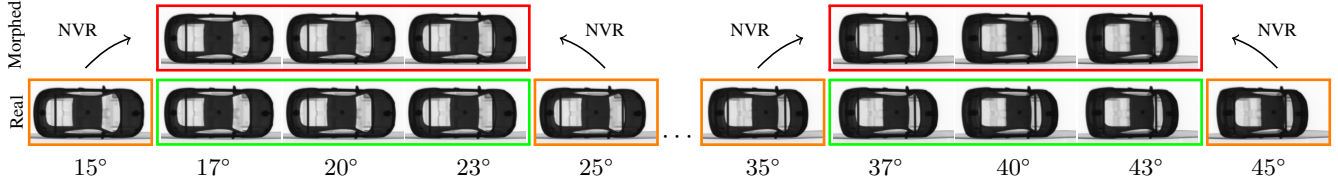


Figure 8: Failure case for image synthesis via our novel view regularizer (NVR) on the CT scan toy car. Given sparse view measurements (orange), we estimated unknown views (red) using proposed flow based morphing algorithm. Compared to ground truth measurements (green), though our approach preserves some important image features at boundary, features (such as bumper inside the toy car at 40°and 43°) is missing since our observations for visible light tomography are not valid.

References

- [1] J. Du, G. Zang, B. Mohan, R. Idoughi, J. Sim, T. Fang, P. Wonka, W. Heidrich, and W. Roberts. Study of spray structure from non-flash to flash boiling conditions with space-time tomography. *International Symposium on Combustion*, 2020. [1](#)
- [2] P. Getreuer. Rudin-Osher-Fatemi total variation denoising using split bregman. *Image Processing On Line*, 2:74–95, 2012. [1, 2, 6](#)
- [3] J. Gregson, M. Krimerman, M. B. Hullin, and W. Heidrich. Stochastic tomography and its applications in 3D imaging of mixing fluids. *ACM Trans. Graph.*, 31(4):52–1, 2012. [5, 6](#)
- [4] M. Okabe, Y. Dobashi, K. Anjyo, and R. Onai. Fluid volume modeling from sparse multi-view images by appearance transfer. *ACM Trans. Graph.*, 34(4):93, 2015. [1, 2, 6](#)
- [5] J. Solomon, F. De Goes, G. Peyré, M. Cuturi, A. Butscher, A. Nguyen, T. Du, and L. Guibas. Convolutional wasserstein distances: Efficient optimal transportation on geometric domains. *ACM Transactions on Graphics (TOG)*, 34(4):66, 2015. [1, 2, 6](#)
- [6] M. Yan. Convergence analysis of SART: optimization and statistics. *International Journal of Computer Mathematics*, 90(1):30–47, 2013. [6](#)
- [7] G. Zang, M. Aly, R. Idoughi, P. Wonka, and W. Heidrich. Super-resolution and sparse view CT reconstruction. In *Proceedings of the European Conference on Computer Vision (ECCV)*, pages 137–153, 2018. [2](#)
- [8] G. Zang, R. Idoughi, R. Tao, G. Lubineau, P. Wonka, and W. Heidrich. Space-time tomography for continuously deforming objects. *ACM Trans. Graph.*, 37(4):36, 2018. [2](#)
- [9] G. Zang, R. Idoughi, R. Tao, G. Lubineau, P. Wonka, and W. Heidrich. Warp-and-project tomography for rapidly deforming objects. *ACM Trans. Graph.*, 38(4), 2019. [1, 2, 3, 4, 5, 6](#)